Effect of FeO concentration in sinter iron ore on reduction behavior in a hydrogen-enriched blast furnace

Ko-ichiro Ohno[1),✉], *Takayuki Maeda*[1)], *Kazuya Kunitomo*[1)], *and Masashi Hara*[2)]

1) Department of Materials, Faculty of Engineering, Kyushu University, 744 Motooka, Nishi-ku, Fukuoka 819-0395, Japan
2) Kashima Area, East Nippon Works, Nippon Steel Corporation, 3 Hikari, Kashima City, Ibaraki 314-0014, Japan

Abstract: Japan started the national project "COURSE 50" for CO_2 reduction in the 2000s. This project aimed to establish novel technologies to reduce CO_2 emissions with partially utilization of hydrogen in blast furnace-based ironmaking by 30% by around 2030 and use it for practical applications by 2050. The idea is that instead of coke, hydrogen is used as the reducing agent, leading to lower fossil fuel consumption in the process. It has been reported that the reduction behavior of hematite, magnetite, calcium ferrite, and slag in the sinter is different, and it is also considerably influenced by the sinter morphology. This study aimed to investigate the reduction behavior of sinters in hydrogen enriched blast furnace with different mineral morphologies in $CO–CO_2–H_2$ mixed gas. As an experimental sample, two sinter samples with significantly different hematite and magnetite ratios were prepared to compare their reduction behaviors. The reduction of wustite to iron was carried out at 1000, 900, and 800°C in a $CO–CO_2–H_2$ atmosphere for the mineral morphology-controlled sinter, and the following findings were obtained. The reduction rate of smaller amount of FeO led to faster increase of the reduction rate curve at the initial stage of reduction. Macro-observations of reduced samples showed that the reaction proceeded from the outer periphery of the sample toward the inside, and a reaction interface was observed where reduced iron and wustite coexisted. Micro-observations revealed three layers, namely, wustite single phase in the center zone of the sample, iron single phase in the outer periphery zone of the sample, and iron oxide-derived wustite FeO and iron, or calcium ferrite-derived wustite 'FeO' and iron in the reaction interface zone. A two-interface unreacted core model was successfully applied for the kinetic analysis of the reduction reaction, and obtained temperature dependent expressions of the chemical reaction coefficients from each mineral phases.

Keywords: hydrogen; reduction; wustite; hematite; magnetite; calcium ferrite; two-interface unreacted core model; COURSE50

1. Introduction

In the 2020s, there were collective efforts all over the world to move toward a carbon-neutral society. To achieve this goal of sustainable development, CO_2 emissions should be strictly controlled. Japan's annual CO_2 emissions in 2016 were the highest in the industrial sector, with the highest contribution of the steel industry [1]. In ironmaking, large CO_2 emissions are attributed to the use of fossil fuels for the iron ore reduction reaction in the blast furnace. Since the oil crisis of the 1970s, the Japanese steel industry has been investigating processes to reduce CO_2 and save energy. It is challenging to further reduce CO_2 emissions based on contemporary technology.

In response to this situation, Japan started the national project "COURSE 50 (CO_2 Ultimate Reduction in Steelmaking process by innovative technology for cool Earth 50)" for CO_2 reduction in the 2000s. This project aimed to establish a new technology to reduce CO_2 emissions with partially utilization of hydrogen in in blast furnace-based ironmaking by 30% by around 2030 and to use it for practical applications by 2050. The main technology of this project comprises CO_2

emission reduction from a blast furnace and CO_2 separation and recovery. Iron ore reduction technology using hydrogen is especially attractive as a carbon-neutral process for ironmaking [2]. Briefly, instead of coke, it uses hydrogen as a reducing agent to decrease fossil fuel consumption in ironmaking. The reduction rate of iron oxide by H_2 is much higher than that by CO, and it can be expected that the process efficiency will also be better [3].

Recent years, there are many reviews [4–5] of hydrogen ironmaking technologies. These reviews were reported comprehensions about hydrogen effect for industrial size furnace and lab scale experiments. Their broad review is worthful to understand hydrogen utilization situation for ironmaking with not only blast furnace. However, it is unclear about sintered iron ore behavior in hydrogen enriched condition in blast furnace reduction conditions.

Because of the considerable demand for crude steel production in emerging countries in East Asia, the quality of raw materials used for blast furnace operation in Japan has worsened. This has led to the depletion of high-grade iron ore and increase of low-grade iron ore. Low-grade iron ore requires mineral processing because of the large amount of

gangue components and combined water. Mineral processing changes ore into fine ore, which cannot be directly used as a raw material for blast furnaces, but it can be used as raw material for pellets or sintered iron ore, hereinafter referred to as sinter. Sinter accounts for approximately 73% of iron ore charged in blast furnaces in Japan [6], and it is crucial to improve the reduction efficiency of sinter in blast furnace operation. It has been reported that different minerals, such as hematite, magnetite, calcium ferrite, and slag, in the sinter have different reduction behaviors, and these are considerably influenced by sinter iron ore morphologies.

Qie *et al.* [7] reported effect of hydrogen on reduction kinetics of iron oxides in blast furnace. They were especially focused on reduction kinetics of iron ore pellet, not sintered iron ore, in whole reduction steps. Although Murakami *et al.* [8] focused on reduction behavior of sintered iron ore, their target is degradation behavior with mineral morphology variations in relatively lower temperature condition. Higuchi *et al.* [9] investigated not only reduction behavior but also soften and melting behavior with reduction test under the loading condition. Although they well explained about gas permeability in packed bed sintered iron ore layer with their reduction and soften behavior, it was not included enough discussions about reduction kinetics in critical reduction step of FeO to Fe.

This study aimed to investigate the reduction behavior of sinter with different mineral morphologies in $CO–CO_2–H_2$ mixed gas. Herein, the focus was on reduction from wustite to in the iron ore reduction reaction because it accounts for approximately 70% of the total weight of oxygen to be reduced.

2. Experimental

2.1. Samples

In this experiment, two samples of sinter provided by the sinter pot test in Nippon Steel were used, as shown in Table 1.

Table 1.   Chemical composition of iron ore sinter   wt%

Sample	T.Fe	FeO	CaO	SiO_2	Al_2O_3
Sample A	57.2	6.19	10.0	5.58	1.70
Sample B	57.4	12.1	10.0	5.72	1.69

The main difference between the two samples was the FeO concentration, and proportions of other components were almost the same. To investigate the effect of FeO concentration on the morphology of the sinter, the area ratios of the pores and each mineral phase were quantified using image processing software, Image J. Each sample was embedded in epoxy resin, cut horizontally to obtain cross sections, and polished using emery paper (Nos. 0–3000) and diamond paste (3 μm, 1 μm) and then observed using an optical microscope. Next, using the image processing software, the pores of the structure in the visual field and the area ratio of each mineral structure were quantified. The area ratio was quantified using optical micrographs taken at 50 times for quanti-

fication of pores and 200 times for quantification of mineral phases. Nine arbitrary fields of view were observed for one sample, and this operation was performed for nine samples. The area ratio of the mineral phases of the sample was the average value from 81 fields of view.

Table 2 shows the measurement results of the pore and mineral phase ratios of each sinter. The mineral phase ratio was quantified by setting the sum of the hematite, magnetite, calcium ferrite, and slag ratios, excluding the pores, to 1. The hematite ratio of Sample A was larger than that of Sample B, and the magnetite ratio of Sample A was smaller than that of Sample B. There was no significant difference in the proportions of calcium ferrite and slag between the two samples. Thus, two sinter samples with significantly different hematite and magnetite ratios could be obtained to compare their reduction behaviors. For the reduction experiment, the sintered ores of Samples A and B were crushed and carved into a 12 mm diameter sphere using a grinder.

Table 2.   Area ratio of mineral phase and pore   %

Sample	Hematite	Magnetite	Calcium ferrite	Slag	Pore
Sample A	33.5	14.6	28.5	23.3	34.0
Sample B	30.4	19.2	29.7	20.7	31.7

2.2. Apparatus

Fig. 1 shows a schematic of the thermobalance with a reaction tube (inner diameter = 35 mm) that was used as the experimental equipment for the reduction experiment. N_2, CO, CO_2, and H_2 were used in the experiments. The flow rate of each gas was adjusted using a mass flow controller. Weight change of the sample during reduction was measured using a strain gauge on the upper part of the thermobalance.
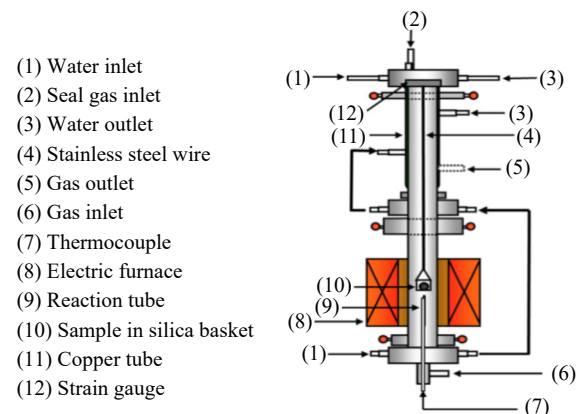
(1) Water inlet
(2) Seal gas inlet
(3) Water outlet
(4) Stainless steel wire
(5) Gas outlet
(6) Gas inlet
(7) Thermocouple
(8) Electric furnace
(9) Reaction tube
(10) Sample in silica basket
(11) Copper tube
(12) Strain gauge

Fig. 1.   Schematic view of experimental apparatus.

2.3. Method

A reduction experiment was conducted using the sample described in Section 2.1. The initial sample whose weight was measured was placed in a silica basket (diameter of approximately 20 mm, height of approximately 16 mm, and weight of approximately 3.8 g), and the weight of the whole setup, including the sample and basket, was measured. The

basket was placed in the isothermal zone of the reaction tube by hanging with a platinum wire.

First, N_2 seal gas (99.99%, 8.33×10^{-6} m$^3\cdot$s^{-1}) was used to protect the thermobalance, N_2 gas (99.99%, 3.33×10^{-5} m$^3\cdot$s^{-1}) was flowed, and the temperature was raised to a pre-determined value (1000, 900, and 800°C). Next, the gas was switched to a 50%CO–50%CO_2 mixed gas, and preliminary reduction was performed until the weight change disappeared, in order to pre-reduce the sample to wustite. Additionally, wustite formation was confirmed with XRD analysis of quenched sample in this step. After prereduction, the gas atmosphere was switched to a predetermined one, as listed in Table 3, for reduction from wustite to iron. The gas flow rate was 3.33×10^{-5} m$^3\cdot$s^{-1} for both prereduction and main reduction.

Table 3.   Reducing gas compositions   vol%

H_2	CO	CO_2
0	90	10
25	67.5	7.5
50	45	5
75	22.5	2.5
100	0	0

The reduction rate was calculated using the following formula:

$$F = \Delta W / W \tag{1}$$

where F is the reduction rate, ΔW is the amount of weight change of the sample (g), and W is the weight of oxygen to be reduced at the reduction stage from wustite to iron (g).

In addition, to investigate the reaction morphology, reduction-interrupted samples with a 60% reduction ratio were prepared under each reduction condition. The reduction changed the sample cross-section, which was obtained using the method mentioned in Section 2.1. The sample was observed via macroscopic observation using a digital camera and microscopic observation using an optical microscope.

3. Results and discussions

3.1. Wustite to iron reduction rate

Figs. 2–4 show the reduction ratio curves from wustite to iron at the reduction temperatures of 1000, 900, and 800°C for Sample A.

Figs. 5–7 show the reduction rate curves from wustite to iron at the reduction temperatures of 1000, 900, and 800°C for Sample B.

At 800°C for both Samples A and B with all gas compositions except for 100% H_2, the carbon precipitation reaction represented by Eqs. (2) and (3) was observed at a reduction rate of approximately 75%.

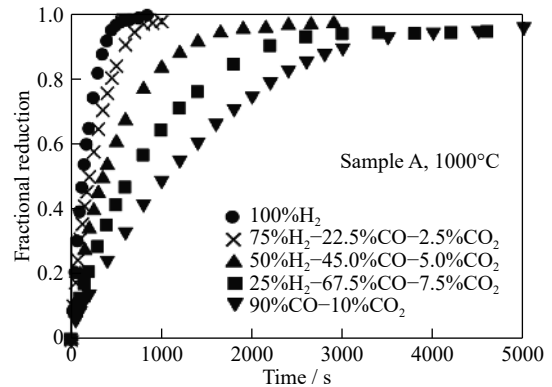To avoid precipitation, the reduction was interrupted at a 60% reduction ratio.

$$CO + H_2 = C + H_2O \tag{2}$$

$$2CO = C + CO_2 \tag{3}$$

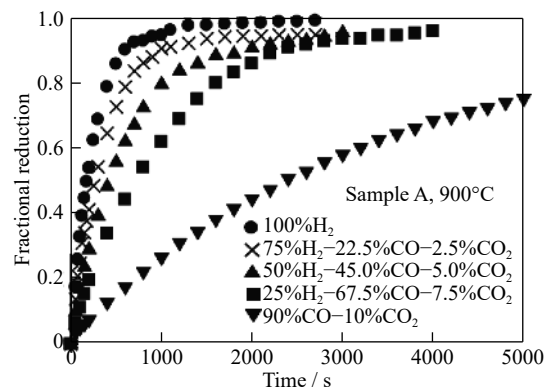**Fig. 2.   Reduction curves of Sample A reduced from FeO to Fe at 1000°C.**

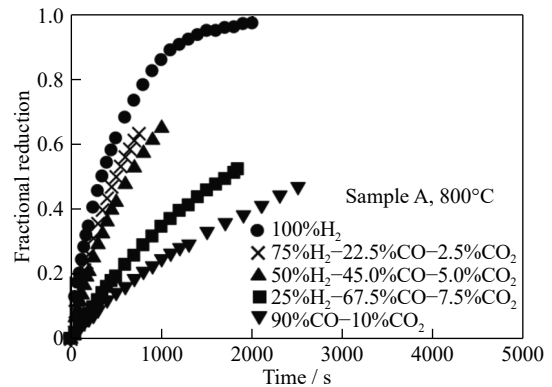**Fig. 3.   Reduction curves of Sample A reduced from FeO to Fe at 900°C.**

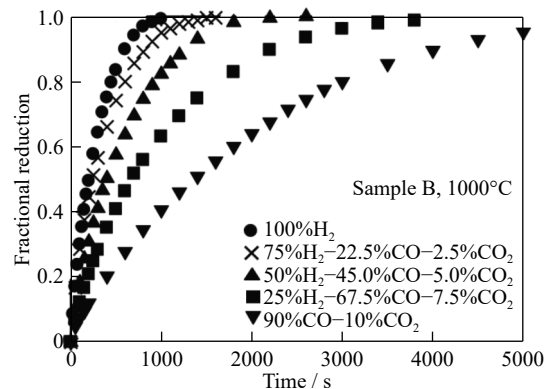**Fig. 4.   Reduction curves of Sample A reduced from FeO to Fe at 800°C.**

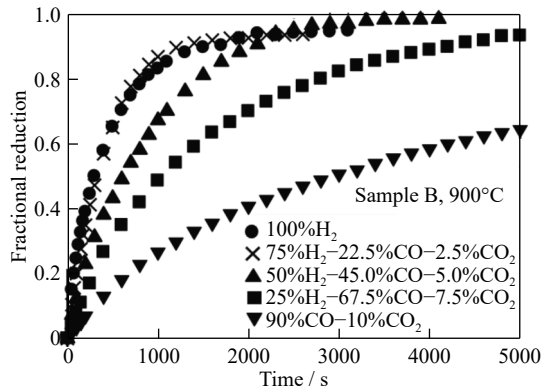**Fig. 5.   Reduction curves of Sample B reduced from FeO to Fe at 1000°C.**

Fig. 6.   Reduction curves of Sample B reduced from FeO to Fe at 900°C.
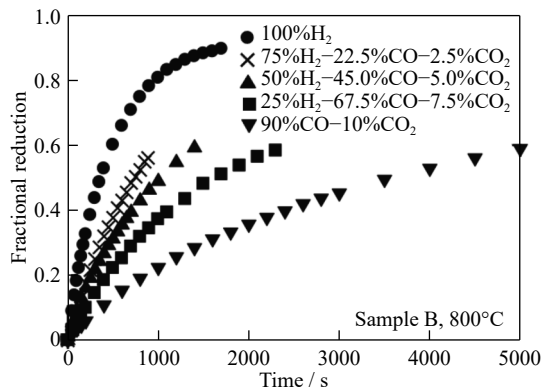

Fig. 7.   Reduction curves of Sample B reduced from FeO to Fe at 800°C.

According to Figs. 2–7, the reduction rate increased as the H_2 concentration increased at all temperatures in both Samples A and B. In addition, the higher the H_2 concentration, the greater the slope of the reduction rate curve at the initial stage of reduction. Based on these reduction rate curves, the slope of the tangent to the reduction rate curve at a reduction rate of 40% was defined as the 40% reduction rate, and the relationship between the reduction rate and H_2 concentration in the bulk gas was investigated.

Figs. 8–10 show the relationship between the reduction rate at reduction temperatures of 1000, 900, and 800°C and the H_2 concentration in the bulk gas; in these figures, the relationships for Samples A and B are compared.
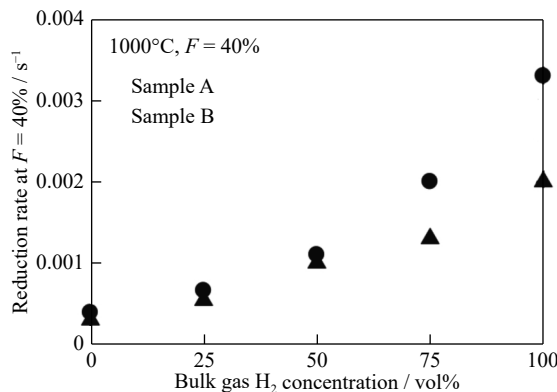

Fig. 8.   Relation between the bulk gas hydrogen concentration and reduction rate at $F = 40\%$, at 1000°C.
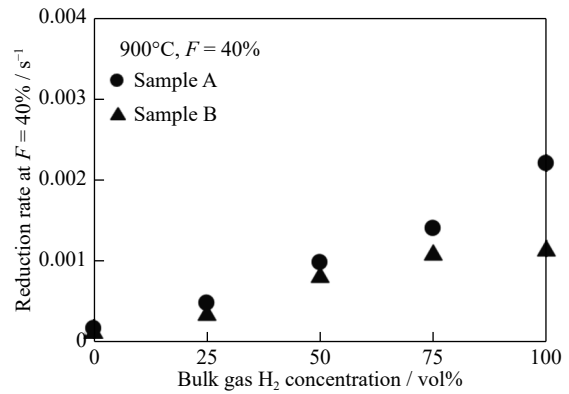

Fig. 9.   Relation between the bulk gas hydrogen concentration and reduction rate at $F = 40\%$, at 900°C.
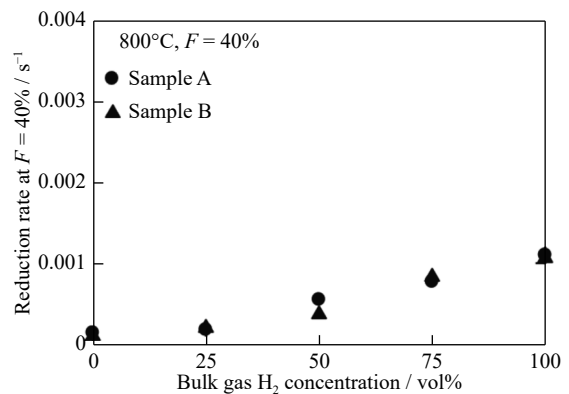

Fig. 10.   Relation between the bulk gas hydrogen concentration and reduction rate at $F = 40\%$, at 800°C.

It was found that the higher the H_2 concentration, the higher the reduction rate; moreover, the higher the reduction temperature, the higher the reduction rate. Furthermore, when comparing each sample, it was found that the reduction rate of Sample A, which has a small amount of FeO, is higher than that of Sample B.

As listed in Table 2, the hematite ratio of Sample A is larger than that of Sample B, and the magnetite ratio of Sample A is smaller than that of Sample B. It is considered that the reducibility of the hematite phase is higher than that of the magnetite phase. Therefore, Sample A showed a better reduction behavior than Sample B. This trend is evident with higher H_2 concentrations and reduction temperatures. Therefore, in order to improve the reduction efficiency of sinter when using hydrogen for iron ore reduction, the amount of FeO should be small to produce sinter with a higher hematite content.

3.2. Observation of reduction-interrupted sample

3.2.1. Macro observation

To investigate the reduction reaction morphology, reduction-interrupted samples were prepared under each reduction condition, and cross-sectional observations were performed for each sample. Figs. 11 and 12 show the macro-observation results of Samples A and B at each reduction temperature, respectively.
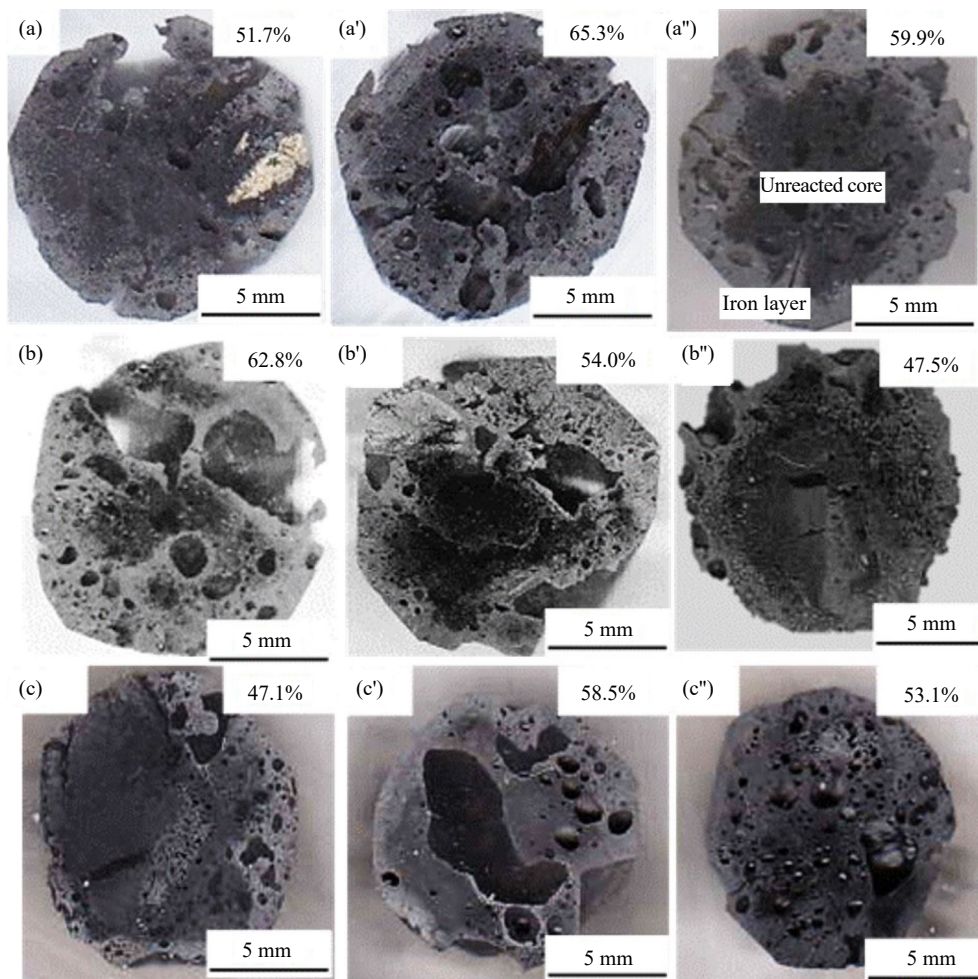
Fig. 11. Cross-sectional view of Sample A partially reduced with $CO–CO_2–H_2$ gas mixture: reduced with $90\%CO–10\%CO_2$ at (a) 1000, (a') 900, and (a'') 800°C; reduced with $50\%H_2–45\%CO–5\%CO_2$ at (b) 1000, (b') 900, and (b'') 800°C; reduced with 100% H_2 at (c) 1000, (c') 900, and (c'') 800°C.

The number indicated by "%" in the figures represents the reduction ratio. From these figures, it was found that the boundary between the reacted layer and the unreacted core existed in the reduction-interrupted sample at each reduction temperature, and the reaction proceeded topochemically. In addition, Samples A and B had similar reaction forms, and no significant differences were observed.

3.2.2. Micro observation

To investigate the microscopic reaction morphology, the reduction-interrupted sample was observed using an optical microscope. The microstructure observation was focused on locations near the sample surface, at the reaction interface, and at the center of the sample. Figs. 13 and 14 show the micro-observation results for Samples A and B, respectively, which were reduction-interrupted at 1000°C.

For Sample A, near the sample surface area, unreduced wustite was negligibly observed in the reduced iron layer using 100% H_2 (Fig. 13(a)). On the other hand, the residual amount of unreduced wustite increased with a lower concentration of hydrogen in the reducing gas (Fig. 13(a') and (a'')). Sample B also showed the same trend as in Fig. 14(a), (a'), and (a''). The amount of unreduced wustite was higher in Sample B than in Sample A, and more unreduced wustite

surrounded by dense reduced iron was observed. This observation is considered to be related to the larger amount of magnetite in Sample A before reduction than in Sample B.

Most of the remaining unreduced wustite is assumed to be hematite or magnetite-derived wustite, not calcium-ferrite-derived wustite. The FeO derived from hematite and 'FeO' derived from calcium ferrite exhibited pores that were generated during reduction to iron, but the FeO derived from magnetite was surrounded by dense reduced iron, and exhibited no pore formation. Fig. 13(b), (b'), (b'') and Fig. 14(b), (b'), (b'') indicate that reduced iron and unreduced wustite are present in the same amount at the reaction interface regardless of the reduced gas composition.

With regard to the unreduced wustite, in addition to hematite or magnetite-derived wustite, calcium ferrite-derived wustite 'FeO' was also observed; this observation is different from that near the sample surface area. Fig. 13(c), (c'), (c'') and Fig. 14(c), (c'), (c'') show that in the core of the sample, most of the structure is unreduced wustite with a small amount of reduced iron, regardless of the reduced gas composition. Microscopic observations of Samples A and B at reduction temperatures of 900 and 800°C showed almost same trend. Thus, the lower reduction rate of Sample B possibly
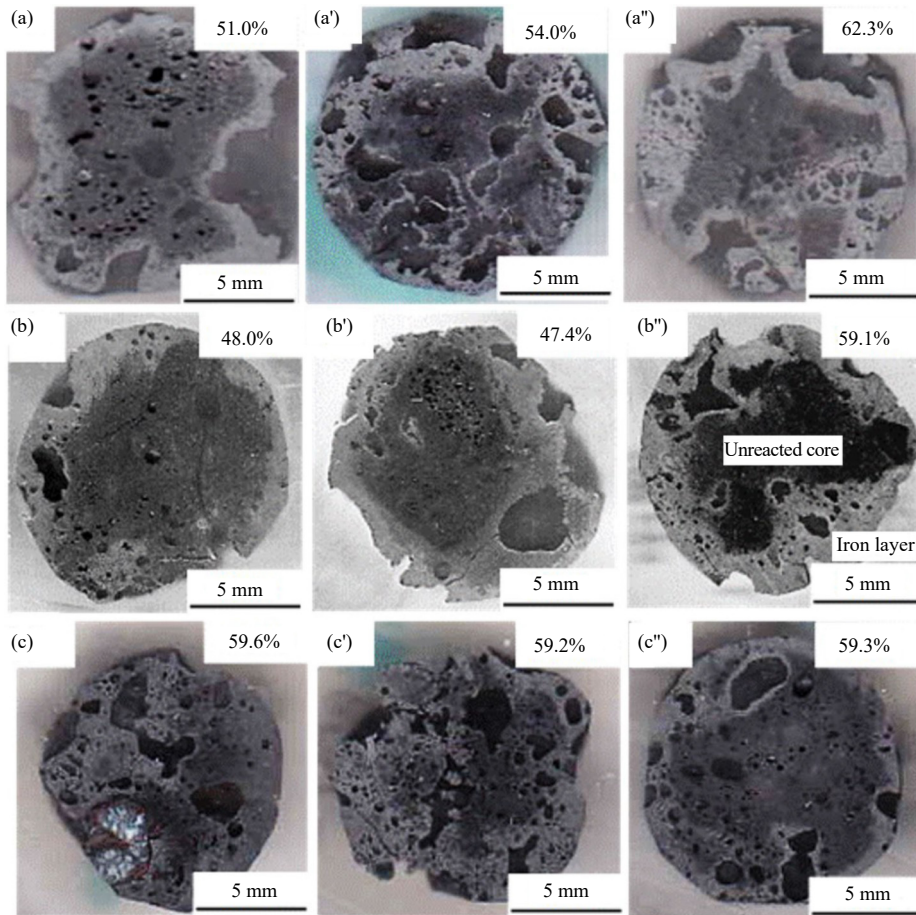
Fig. 12. Cross-sectional view of Sample B partially reduced with CO–CO$_2$–H$_2$ gas mixture: reduced with 90%CO–10%CO$_2$ at (a) 1000, (a') 900, and (a'') 800°C; reduced with 50%H$_2$–45%CO–5%CO$_2$ at (b) 1000, (b') 900, and (b'') 800°C; reduced with 100% H$_2$ at (c) 1000, (c') 900, and (c'') 800°C.
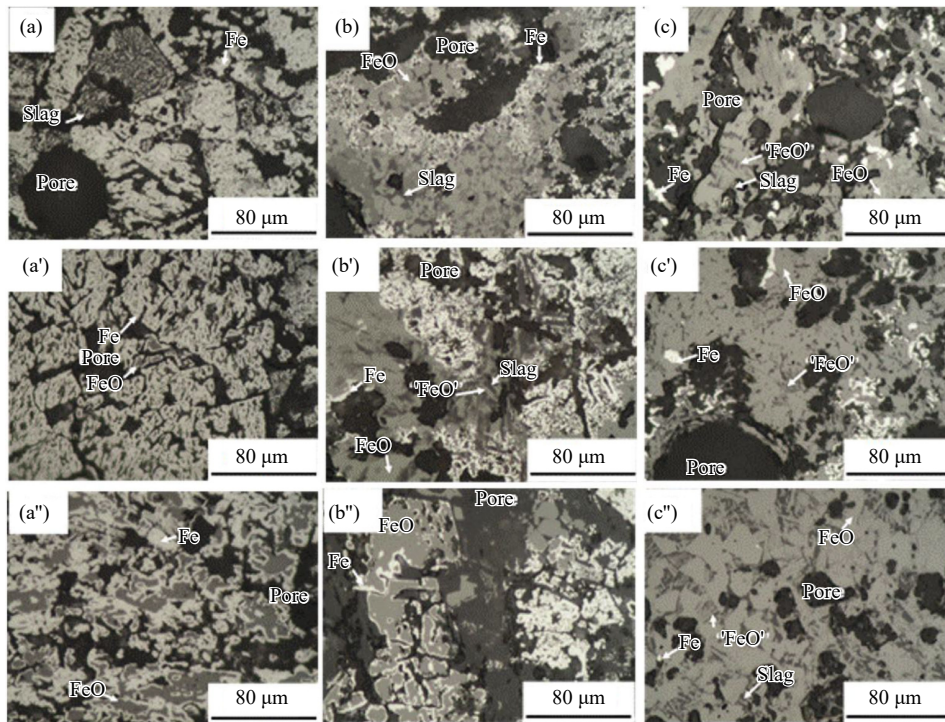

Fig. 13. Microstructure of Sample A partially reduced at 1000°C (Fe : Reduced iron; FeO : Wustite derived from iron oxide; 'FeO': Wustite derived from calcium ferrite): reduced with 100% H$_2$ at (a) periphery part, (b) reaction interface, and (c) center part; reduced with 50%H$_2$–45%CO–5%CO$_2$ at (a') periphery part, (b') reaction interface, and (c') center part; reduced with 90%CO–10%CO$_2$ at (a'') periphery part, (b'') reaction interface, and (c'') center part.
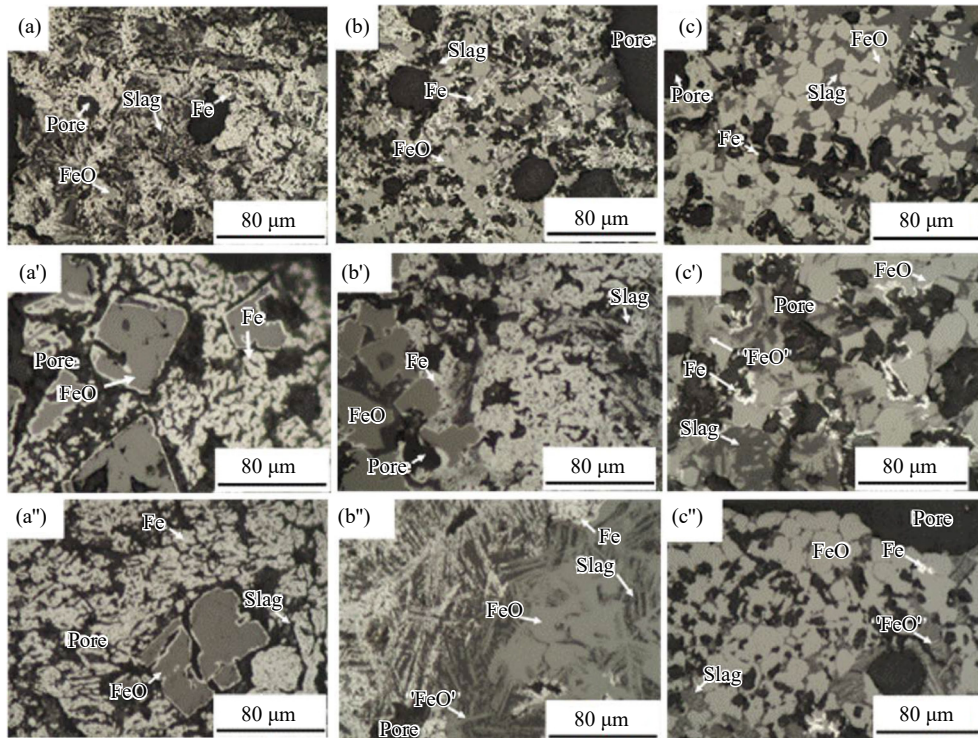
Fig. 14.   Microstructure of Sample B partially reduced at 1000°C (Fe : Reduced iron; FeO : Wustite derived from iron oxide; 'FeO': Wustite derived from calcium ferrite): reduced with 100% H₂ at (a) periphery part, (b) reaction interface, and (c) center part; reduced with 50%H₂–45%CO–5%CO₂ at (a') periphery part, (b') reaction interface, and (c') center part; reduced with 90%CO–10%CO₂ at (a'') periphery part, (b'') reaction interface, and (c'') center part.

arises from the surrounding dense reduced iron on the unreduced wustite near the surface of Sample B. The surrounding dense iron layer could hinder gas diffusion toward the unreacted core. This inhibition of gas diffusion in Sample B resulted in a lower reduction rate than Sample A.

4. Reduction rate analysis

From the macro-observation results for the reduction-interrupted sample in Section 3.2.1, it was found that the reaction topochemically proceeded from the outer periphery toward the inside. From the microscopic observation results for the reduction-interrupted sample in Section 3.2.2, the outer peripheral part was almost a single phase of reduced iron. Reduced iron coexisted with iron oxide-derived wustite FeO or calcium ferrite-derived wustite 'FeO' in the reaction interface, while FeO and 'FeO' coexisted in the unreacted core. Therefore, in this study, an unreacted core model was applied for the reduction of FeO and 'FeO'. Various models have been employed for the reduction rate analysis of sinter. Typical models include the one-interface unreacted core model [10], intermediate model [11–12], and grain model [13–14]. In the case of iron ore reduction, the aforementioned models consider the reduction reactions of interest as wustite-to-iron reduction reactions and hematite-to-iron stepwise reduction reactions.

However, since the sinter contains multiple mineral phases with different reduction equilibria, such as hematite, magnetite, and calcium ferrite, it is not possible to conduct an accurate rate analysis with these models. In other words,

there is a need for a novel and suitable estimation model for the accurate kinetic analysis of the reduction reaction rate of complex agglomerates, including dissimilar mineral phases such as sinter. Noguchi *et al*. [15] developed a new two-interface unreacted core model. This model is based on the multi-interface model by Spitzer *et al*. [16]. One of the focus areas of this study was to determine whether or not Noguchi's model could be used for the reduction rate analysis of sinter.

In the two-interface unreacted core model, the parameters required for analysis are the gas transfer coefficient (k_f (m·s^{-1})), effective diffusion coefficient of the outer shell layer (D_e^{out} (m²·s^{-1})), effective diffusion coefficient of the inner shell layer (D_e^{in}), and chemical reaction rate constant (k_C (m·s^{-1})). Among them, the mass transfer coefficient in the gas boundary film uses the k_f from the Ranz-Marshall equation [17] considering the balance resistance [18]; k_C can be calculated from the k_C^0 of the single mineral sample and the mineral ratio in the sinter. In this study, D_e^{out} and D_e^{in} were used as parameters, and parameter fitting was carried out to minimize the square of the difference between the reduction rate obtained by the calculation model and experiment. $D_e^{out} \geq D_e^{in}$ was set as the fitting condition because the porosity of the inner shell layer is considered to be lower than that of the outer shell layer.

The following equation was used for the equilibrium constant K required for the analysis.

Equilibrium constant from iron oxide–derived FeO to iron [19]:

CO–CO$_2$ system : $K_{CO} = T^{0.9262}\exp(-10.08 - 3218/T)$
(873–1623 K)   (4)

H$_2$–H$_2$O system : $K_{H_2} = \exp(0.973 - 1743/T)$
(873–1600 K)   (5)

Equilibrium constant from calcium ferrite–derived 'FeO' to iron [20]:

CO–CO$_2$ system : $K_{CO} = \exp(-2.785 - 2042/T)$
(1073–1323 K)   (6)

H$_2$–H$_2$O system : $K_{H_2} = \exp(0.8648 - 1709/T)$
(1073–1373 K)   (7)

The apparent chemical reaction rate constant of the oxide in the mixture is proportional to the abundance ratio of the oxide [21]. The chemical reaction rate constant of the oxide "s" in the oxide mixture $k_C^{(s)}$ is expressed by Eq. (8) using the chemical reaction rate constant $k_C^{(s)°}$ (m·s^{-1}) of pure "s" and the abundance ratio $\phi^{(s)}$ of the oxide "s".

$$k_C^{(s)} = k_C^{(s)°}\phi^{(s)}$$ (8)

In this study, as the chemical reaction rate constants $k_C^{(s)°}$ of FeO and 'FeO', the values obtained by analyzing the experimental results using a single mineral sample with the same experimental equipment and method were used. The temperature-dependent equations for each chemical reaction rate constant can be expressed by Eqs. (9) to (14). The gas constant $R = 8.314$ (J·mol^{-1}·K^{-1}).

Chemical reaction rate constant from hematite-derived FeO to iron:

CO–CO$_2$ system : $k_C^{(s)°} = \exp[5.56 - 49.5 \times 10^3/(RT)]$
(1173–1373 K)   (9)

H$_2$–H$_2$O system : $k_C^{(s)°} = \exp[12.1 - 91.7 \times 10^3/(RT)]$
(1173–1373 K)   (10)

Chemical reaction rate constant from magnetite-derived FeO to iron:

CO–CO$_2$ system : $k_C^{(s)°} = \exp[3.55 - 28.4 \times 10^3/(RT)]$
(1073–1373 K)   (11)

H$_2$–H$_2$O system : $k_C^{(s)°} = \exp[6.22 - 42.7 \times 10^3/(RT)]$
(1073–1373 K)   (12)

Chemical reaction rate constant from calcium ferrite-derived 'FeO' to iron:

CO–CO$_2$ system : $k_C^{(s)°} = \exp[7.14 - 64.5 \times 10^3/(RT)]$
(1073–1373 K)   (13)

H$_2$–H$_2$O system : $k_C^{(s)°} = \exp[9.62 - 78.4 \times 10^3/(RT)]$
(1073–1373 K)   (14)

The relationships between the k_C values and temperature of Sample A and Sample B are shown in Fig. 15 and Fig. 16, respectively.

Both figures indicate that the k_C values in both samples are higher in FeO than in 'FeO', and are higher for H$_2$ reduction than CO reduction. Further, on comparing the k_C values of Sample A and Sample B, that of the former is slightly higher, but the difference is small. Although the abundance ratio of
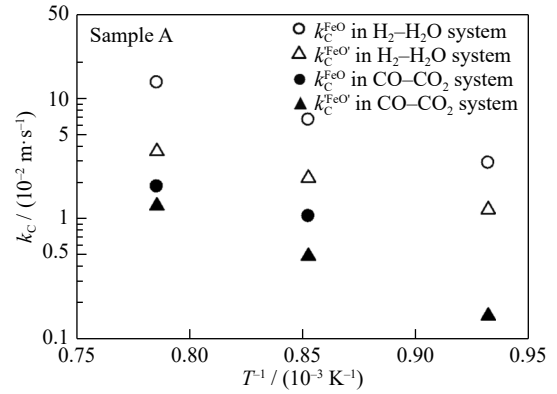

Fig. 15.   Temperature dependency of chemical reaction rate of Sample A.
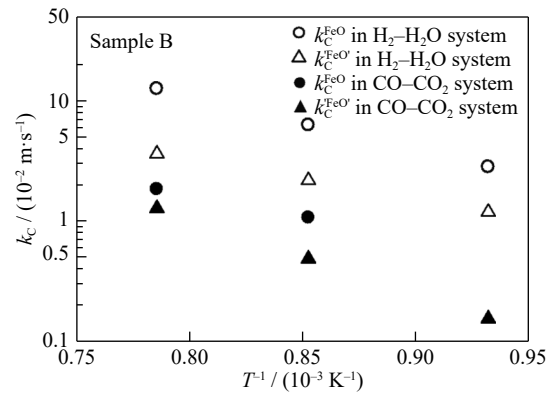

Fig. 16.   Temperature dependency of chemical reaction rate of Sample B.

each mineral based on the values in Table 2 was used when calculating k_C, the difference between the two samples is presumed to not be large enough to affect the calculation of the k_C values.

Since the chemical reaction rate constant for FeO starting from hematite cannot be applied at 800°C (Eqs. (9) and (10)), the analysis was carried out for the results at 900 and 1000°C. Figs. 17 and 18 show the plots of D_e^{out} and D_e^{in} from H$_2$ reduction and CO reduction, obtained by parameter fitting against the reciprocal of temperature.
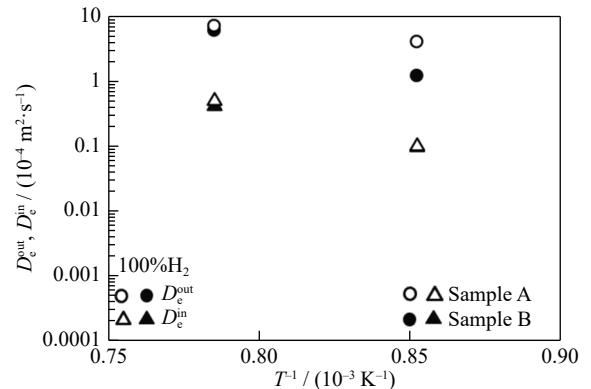

Fig. 17.   Temperature dependency of effective diffusivities D_e^{out} and D_e^{in} with 100% H$_2$ gas.

The figures indicate that D_e^{out} and D_e^{in}, for both, H$_2$ reduction and CO reduction, are higher in Sample A than in

Sample B. Based on the measured values in Table 2, Sample A has a higher porosity than Sample B. This is one of the reasons why the effective diffusion coefficient of Sample A is high. In addition, from the microstructure observations in Figs. 13 and 14, the FeO derived from hematite and 'FeO' derived from calcium ferrite exhibit pore formation during reduction to iron.
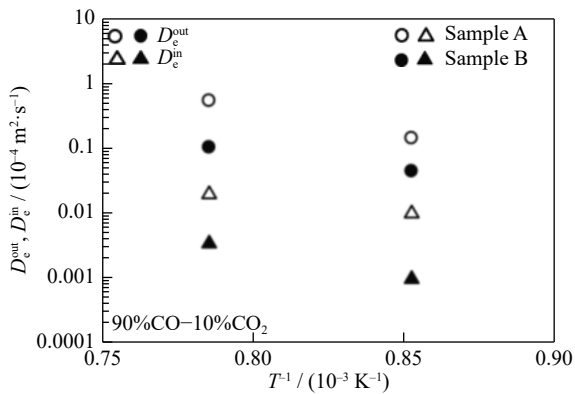

Fig. 18. Temperature dependency of effective diffusivities D_e^{out} and D_e^{in} with 90%CO–10%CO$_2$ gas mixture.

On the other hands, the FeO derived from magnetite is densely reduced and surrounded by iron, exhibiting no pore formation. Sample A contains a small amount of magnetite. This is also considered to be one of the reasons why Sample A has a higher effective diffusion coefficient. Thus, it is considered that the sinter with a high proportion of hematite and calcium ferrite and low proportion of magnetite is advantageous for gas diffusion.

5. Conclusions

A reduction experiment from wustite to iron was conducted at 1000, 900, and 800°C in a CO–CO$_2$–H$_2$ atmosphere for a mineral morphology-controlled sinter, and the following findings were obtained.

(1) By estimating the mineral phase ratio of sinters with different amounts of FeO, it was found that Sample A, with a small amount of FeO, has a larger amount of hematite and smaller amount of magnetite than Sample B.

(2) The reduction rate increases as the H$_2$ concentration increases, and the reduction rate curve at the initial stage of reduction tends to rise faster. In addition, the reduction rate increases as the reduction temperature increases. The smaller the amount of FeO, the faster is the rise of the reduction rate curve at the initial stage of reduction.

(3) Macro-observations indicate that the reaction proceeds from the outer periphery of the sample toward the inside. The reaction interface where reduced iron and wustite coexist is observed. Micro-observations confirm the presence of the following three layers: a single phase of wustite at the center of the sample, a single phase of iron in the outer periphery of the sample, iron oxide-derived wustite FeO and iron, or calcium ferrite-derived wustite 'FeO' and iron in the reaction interface zone.

(4) The two-interface unreacted core model was applied in the kinetic analysis of the reduction reaction. It was found that the reduction rate of the sinter with multiple mineral phases can be analyzed by parameter fitting using the nonlinear least squares method with the interfacial reaction rate constant.

Acknowledgement

Conflict of Interest

The authors declare no conflict of interests.

References

[1] Greenhouse Gas Inventory Office of Japan and Ministry of the Environment, Japan, ed., *National Greenhouse Gas Inventory Report of JAPAN 2022*, Center for Global Environmental Research, Earth System Division, National Institute for Environmental Studies, Japan, 2022.

[2] T. Miwa and H. Okuda, CO$_2$ ultimate reduction in steelmaking process by innovative technology for cool earth 50 (COURSE50), *J. Jpn. Inst. Eng.*, 89(2010), No. 1, p. 28.

[3] S. Ban-Ya, Y. Iguchi, and T. Nagasaka, Rate of reduction of liquid wustite with hydrogen, *Tetsu-to-Hagane*, 70(1984), No. 14, p. 1689.

[4] Y.B. Chen and H.B. Zuo, Review of hydrogen-rich ironmaking technology in blast furnace, *Ironmaking Steelmaking*, 48(2021), No. 6, p. 749.

[5] K.H. Ma, J.Y. Deng, G. Wang, Q. Zhou, and J. Xu, Utilization and impacts of hydrogen in the ironmaking processes: A review from lab-scale basics to industrial practices, *Int. J. Hydrogen Energy*, 46(2021), No. 52, p. 26646.

[6] *Steel Year Book*, Japan Metal Daily, Tokyo, 2014, p. 84.

[7] Y.N. Qie, Q. Lyu, J.P. Li, C.C. Lan, and X.J. Liu, Effect of hydrogen addition on reduction kinetics of iron oxides in gas-injection BF, *ISIJ Int.*, 57(2017), No. 3, p. 404.

[8] T. Murakami, H. Wakabayashi, D. Maruoka, and E. Kasai, Effect of hydrogen concentration in reducing gas on the changes in mineral phases during reduction of iron ore sinter, *ISIJ Int.*, 60(2020), No. 12, p. 2678.

[9] K. Higuchi, S. Matsuzaki, K. Saito, and S. Nomura, Improvement in reduction behavior of sintered ores in a blast furnace through injection of reformed coke oven gas, *ISIJ Int.*, 60(2020), No. 10, p. 2218.

[10] T. Yagi and Y. Ono, A method of analysis for reduction of iron oxide in mixed-control kinetics, *ISIJ Int.*, 8(1968), No. 6, p. 377.

[11] M. Ishida and C.Y. Wen, Comparison of kinetic and diffusional models for solid–gas reactions, *AIChE J.*, 14(1968), No. 2, p. 311.

[12] T. Murayama and Y. Ono, Method of determination of parameters included in ISHIDA-WEN'S model, *Tetsu-to-Hagane*, 73(1987), No. 10, p. 1323.

[13] J. Szekely and J.W. Evans, A structural model for gas—Solid reactions with a moving boundary, *Chem. Eng. Sci.*, 25(1970), No. 6, p. 1091.

[14] J. Szekely and J.W. Evans, A structural model for gas–solid re-

actions with a moving boundary-II: The effect of grain size, porosity and temperature on the reaction of porous pellets, *Chem. Eng. Sci.*, 26(1971), No. 11, p. 1901.

[15] D. Noguchi, K.I. Ohno, T. Maeda, K. Nishioka, and M. Shimizu, Kinetics of reduction step of wustite to iron of hematite and quaternary calcium ferrite mixtures, *Tetsu-to-Hagane*, 98(2012), No. 2, p. 55.

[16] R.H. Spitzer, F.S. Manning, and W.O. Philbrook, Generalized model for the gaseous, topochemical reduction of porous hematite spheres, *Trans. Metall. Soc. AIME*, 236(1966), p. 1715.

[17] W.E. Ranz and W.R. Marshall, Evaporation from drops, part I, *Chem. Eng. Prog.*, 48(1952), No. 3, p. 141.

[18] H.W. St. Clair, Rate of reduction of an oxide sphere in a stream of reducing gas, *Trans. Metall. Soc. AIME*, 233(1965), p. 1145.

[19] T. Usui, M. Naito, T. Murayama, and Z.I. Morita, Kinetic analysis on gaseous reduction of agglomerates, part 1, reaction models for gaseous reduction of agglomerates, *Tetsu-to-Hagane*, 80(1994), No. 6, p. 431.

[20] T. Maeda and Y. Ono, Kinetics of reduction step of wustite to iron in gaseous reduction of quaternary calcium ferrite, *Tetsu-to-Hagane*, 77(1991), No. 10, p. 1569.

[21] T. Murayama, Y. Ono, and C. Kamijo, Effect of the amount of gangue on rate parameters included in the unreacted-core model, *CAMP-ISIJ*, 2(1989), No. 4, p. 949.